Decoupling Control of Multiactive Bridge Converters Using Linear Active Disturbance Rejection

Bandyopadhyay, S.; Qin, Z.; Bauer, P.

DOI
10.1109/TIE.2020.3031531

Publication date
2020

Document Version
Accepted author manuscript

Published in
IEEE Transactions on Industrial Electronics

Decoupling Control of Multi-Active Bridge Converters using Linear Active Disturbance Rejection

Soumya Bandyopadhyay, *Student Member, IEEE,* Zian Qin, *Senior Member, IEEE,* and Pavol Bauer, *Senior Member, IEEE*

***Abstract*—Multi-active bridge converter (MAB) is a promising solution for integrating multiple renewable sources, storage, and loads for various applications. However, the MAB converter is challenging to control due to the inherent coupling between the port power flows. To that end, this paper presents a decoupling control strategy based on linear active disturbance rejection control (LADRC). The proposed controller observes the coupling disturbance using a linear extended state observer (LESO) and subsequently rejects the observed disturbance resulting in dynamic decoupling. Experiments conducted on a 2-kW 100 kHz Si-C based four-port MAB converter laboratory prototype illustrates the decoupling performance of the proposed control strategy. Compared to the traditional decoupling control strategy, the proposed approach is decentralized and model-independent, only requiring information regarding its order.**

***Index Terms*—Active disturbance rejection control, DC-DC converter, decoupled power flow control, disturbance observer, multi-active-bridge converter.**

I. Introduction

MULTI-Port Converter (MPC) is seen as a potential solution for different energy management systems requiring integrating diverse renewable or conventional energy sources, storage systems, and loads [1]. Therefore, MPCs have seen many potential fields of application like more electric aircraft or all-electric ship [2]–[4], electric vehicle (EV) charging applications [5]–[7], energy router for smart homes [8] etc. The advantages of multi-port converters are 1) reduced component requirement, 2) quick dynamic response, and 3) high system efficiency and power density. One of the promising topologies in the multi-port converter family is the multi-active bridge (MAB) converter. The MAB converter consists of multiple bridges (half-bridge or full-bridge) connected via a high-frequency (HF) multi-winding transformer [8]–[10]. Derived from the dual-active bridge (DAB) converter family [11], the MAB converter not only integrates and exchanges the energy from/to all ports, but also provides full isolation among all ports and matches the different port voltage levels.

A key challenge in the MAB converter's design and control is the inherent cross-coupling of power flows between ports. Therefore, the MAB converter behaves as a multi-input multi-output (MIMO) system with coupled power loops, difficult to control. In the literature, several control techniques to decouple the power flows are reported. A pre-compensator based control method is proposed in [12], which decouples the control loops dynamically with pre-calculated gain matrices stored as a look-up table in the controller. Another control technique decouples the control loops by choosing different bandwidths for the SISO loops [8], [13], [14]. Therefore, the loop with the highest bandwidth determines the phase-shift direction during transients. A hybrid approach combining the above two methods is reported in [4] for applications like more-electric aircraft (MEA) to integrate storage systems with different dynamic behavior. A time-sharing control strategy is reported in [10], [15], which decouples the power flows by operating the MAB converter as a DAB converter with only two active ports and other ports deactivated as diode rectifiers at any particular time. However, the device stress and the voltage ripple associated with this control technique are usually high, which leads to larger filtering capacitors. As mentioned above, the control techniques are challenging to

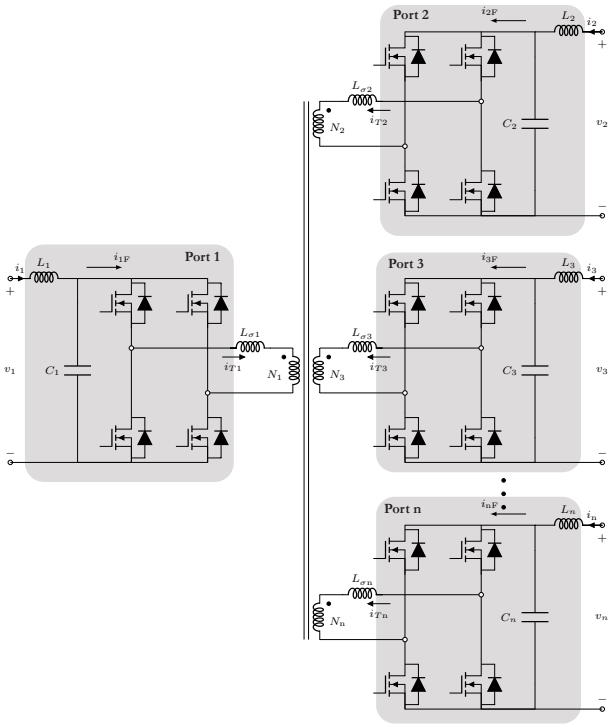

Figure 1: Topology of a multi-active bridge (MAB) converter.

All authors are with the Department of Electrical Sustainable Energy, DCE&S group, TU Delft, Mekelweg 4, 2628 CD, Delft, the Netherlands. The corresponding author is Zian Qin (z.qin-2@tudelft.nl).

This work is part of the research programme P 13-21 with project number A, which is financed by the Netherlands Organisation for Scientific Research (NWO).

implement due to their computational complexity or hardware challenges, or requirement of component information that might change during an operational lifetime. Thus, they inhibit the scalability of the number of ports in MAB converters and reduces their applicability.

Therefore, it is of significant research interest to develop a control algorithm which achieves dynamic decoupling of MAB converters in a decentralized way and requires minimal information. One way to address this is by introducing an observer of the coupling disturbance into the ports' controller design in the MAB converter. If one can observe the disturbance due to coupling sufficiently fast, then the controller can reject it. This technique is known as active disturbance rejection control (ADRC). ADRC is a relatively new control concept proposed as an alternative to traditional PI or PID control [16]–[18]. The ADRC control strategy's concept is to observe the controller's internal and external disturbances in real-time and actively compensate for them. The main strength of ADRC is that it is essentially model-independent and only requires information regarding the order of the plant [19]–[22]. Traditionally, ADRC uses non-linear feed-back gains for better performance. In this paper, a linear active disturbance rejection control (LADRC) is used as it is more simple to implement and tune [23]. LADRC has been used in power electronics applications for output voltage regulation of converters by rejecting disturbances or uncertainties due to load resistance changes [17], input voltage variations, circuits parametric uncertainties, and other external disturbances [19], [24]. This paper presents a linear active-disturbance rejection control approach for decoupling a multi-active bridge converter's power flows. The cross-coupling between the port controllers is formulated as a disturbance in the individual ports' ADRC controller. A linear extended state observer (LESO) is designed for each MAB port to observe the disturbance due to coupling. The observed disturbance is then actively compensated by the decentralized ADRC controllers in real-time. Thus, dynamic decoupling of the power flows in the MAB converter is achieved. The proposed LADRC approach is implemented on 2 kW, 100 kHz four-port multi-active bridge converter, or a quad-active bridge converter (QAB) prototype for validation purposes. The experimental results illustrate that the proposed control strategy dynamically decouples the power flows. The main advantage of the proposed approach is that it only requires information regarding the system's order, unlike the detailed model-based information needed for the conventional decoupling control (CDC) approach [4], [12]. Besides, once tuned properly, LADRC controllers can dynamically decouple the power flows without changing the controller gains. Further, ADRC based decoupling control is decentralized in nature and enables scalability of the number of MAB ports. In summary, this paper's main contribution compared to previous works is introducing a decoupling control strategy for MAB converters that is model-independent, decentralized, and consequently enables scalability of ports.

The paper is organized into six parts. Section II provides a brief overview of the operational theory of the MAB converter. Section III introduces the ADRC formulation of the decoupling control of the MAB converter. Results obtained from simulations based on a four-port MAB converter or a quad-active bridge converter (QAB) are discussed in Section IV. Section V reports the experimental validation of the proposed control strategy on a QAB converter prototype. Finally, general conclusions are summarized based on the analysis and the results.

II. Operating principle of MAB converters

A. Power flows of MAB converters

Figure 1 presents the topology of an *n*-port MAB converter comprised of *n* full-bridge modules magnetically coupled via an *n*-winding HF transformer. MAB converter is a natural extension of the dual-active bridge (DAB) converter introduced in [11]. A DAB converter can be considered as a MAB converter with two active ports. Therefore, the power flow equations derived for DAB converters can be extended to a MAB converter. The cycle-to-cycle average power transferred between port #i and port #j of a MAB converter is given by:

$$P_{\mathrm{ij}} = \frac{V_{\mathrm{i}}^{'} V_{\mathrm{j}}^{'}}{2\pi f_{\mathrm{sw}} L_{\mathrm{ij}}} \phi_{\mathrm{ij}} \big(1 - \frac{|\phi_{\mathrm{ij}}|}{\pi}\big), \qquad \phi_{\mathrm{ij}} = \phi_{\mathrm{i}} - \phi_{\mathrm{j}} \tag{1}$$

where $V_{\mathrm{i}}^{'}$, $V_{\mathrm{j}}^{'}$ are the port dc voltages; L_{ij} is the equivalent inductance between ports #i and #j; f_{sw} is the switching frequency; ϕ_{ij} is the phase-shift between the two square wave voltages at the corresponding transformer terminals.

For the upcoming analysis, a four-port MAB converter or a quad-active bridge converter (QAB) is considered without any loss of generality. A star-equivalent model (see Figure 2a) is used for analysing the operation and switching conditions of the MAB converter. The ports of the MAB converter in Figure 1 are replaced by rectangular voltages sources in the equivalent circuit, and all the generated ac voltages and ac currents are referred to port #1. The power flows between ports can be controlled by the phase shift angles of the square wave voltages at each port. The voltage of the transformer star-point (V_{x}) can be expressed using the theory of superposition:

$$V_{\mathrm{x}} = \sum_{\mathrm{i}=1}^{n} \frac{\left(\sum\limits_{\mathrm{j}=1,\mathrm{j}\neq\mathrm{i}}^{n} \frac{1}{L_{\sigma\mathrm{j}}^{'}} \right)^{-1}}{L_{\sigma\mathrm{i}}^{'} + \left(\sum\limits_{\mathrm{j}=1,\mathrm{j}\neq\mathrm{i}}^{n} \frac{1}{L_{\sigma\mathrm{j}}^{'}} \right)^{-1}} V_{\mathrm{i}}^{'} \tag{2}$$

Therefore, the current slopes of the transfomer windings of the MAB equivalent circuit can be expressed as the following:

$$\frac{di_{\mathrm{Ti}}^{'}}{dt} = \frac{V_{\mathrm{x}} - V_{\mathrm{i}}^{'}}{L_{\sigma\mathrm{i}}^{'}} \tag{3}$$

The actual transformer currents can be obtained by integrating (3) over a switching period. Figure 2b and 2c show the idealized transformer voltage and current switching waveforms of a QAB converter at a certain operating point.

B. Small signal model of MAB converter

Single-phase shift (SPS) control is used to control the power flows in individual ports. In this modulation strategy, the phase-shift angles (ϕ) of the individual ports are used to

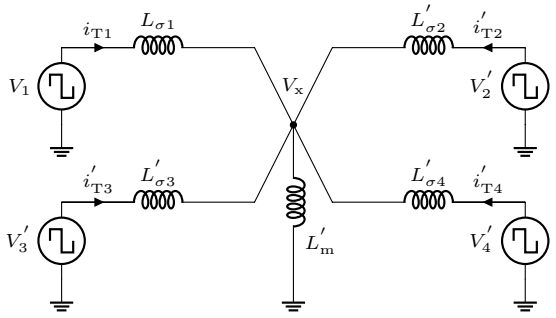

(a)

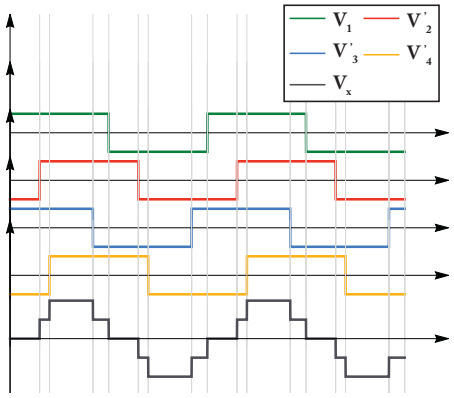

(b)

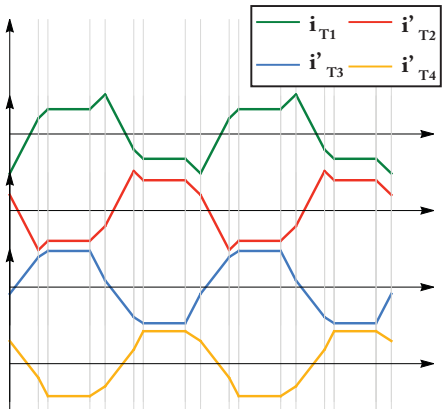

(c)

Figure 2: (a) Equivalent circuit of the QAB converter, (b) idealized steady-state switching waveforms of the transformer voltages with phase shifts, and (c) idealized steady-state transformer current waveforms assuming unity-dc-conversion ratios and equal leakage inductances.

control the inter-port power flows. A linearized small signal gain matrix for a four-port MAB converter [8], [12], [25] at a certain operating point can be represented as:

$$\begin{bmatrix} i_{2F} \\ i_{3F} \\ i_{4F} \end{bmatrix} = \begin{bmatrix} G_{22} & G_{23} & G_{23} \\ G_{32} & G_{33} & G_{34} \\ G_{42} & G_{43} & G_{44} \end{bmatrix} \begin{bmatrix} \phi_2 \\ \phi_3 \\ \phi_4 \end{bmatrix} \tag{4}$$

where i_{iF} ($i \in [1, 4]$) are the pre-filter currents of the dc ports. The dynamics of the dc port currents (i_i) can be obtained combining (4) with the transfer functions of the dc side filters of the QAB ports. The expressions of the gain elements G_{ij} $\forall[i, j]$ in the input to output gain matrix can be expressed as:

$$G_{ij} = \begin{cases} \sum_{p \neq i}^{n} \frac{V_{p,A}}{2\pi f_s L_{ip}} \left(1 - \frac{2|\phi_{i,A} - \phi_{p,A}|}{\pi}\right), & \forall[i = j] \\ -\frac{V_{j,A}}{2\pi f_s L_{ij}} \left(1 - \frac{2|\phi_{j,A} - \phi_{i,A}|}{\pi}\right), & \forall[i \neq j] \end{cases} \tag{5}$$

Since the non-diagonal elements G_{ij} $\forall[i \neq j]$ are all non-zero entities, the resulting control input to output gain matrix **G** becomes a non-diagonal matrix. Therefore, the power flow control of the individual ports are cross-coupled and requires decoupling control technique to achieve good dynamic and stable performance.

C. Conventional decoupling control

The mutual interaction can be eliminated by using a special pre-compensator or decoupling network which decomposes a multivariable control system into a series independent single-loop subsystems. Thus, the system can be controlled via independent loop controllers. This is known as the conventional or traditional decoupling control (CDC) for MAB converters [12].

To achieve independent control loops, the effective input to output gain matrix **X** needs to be a diagonal matrix:

$$X = GH = \begin{bmatrix} x_2 & 0 & 0 \\ 0 & x_3 & 0 \\ 0 & 0 & x_4 \end{bmatrix} \tag{6}$$

Therefore, the decoupling network can be designed as :

$$H = \begin{bmatrix} H_{22} & H_{23} & H_{23} \\ H_{32} & H_{33} & H_{34} \\ H_{42} & H_{43} & H_{44} \end{bmatrix} = G^{-1}X \tag{7}$$

For every operating point, the small signal transfer function matrix of the converter **G** is only a constant, i.e., no pole or zero is involved since the inductor dynamics are already neglected, and so does the decoupling network , which is the inverse matrix of the plant matrix **G**. Therefore, based on the operating point, the elements of the decoupling matrix **H** can be calculated in advance and be stored as lookup tables.

III. LADRC Decoupling of MAB converter

Linear active disturbance rejection control (LADRC) belongs to the class of control algorithms designed to control systems with uncertainities and disturbances [26]. In essence, ADRC uses an observer to track disturbances in real-time and actively compensates for it. Therefore, it has found use in a wide range of industrial application like mechatronics, chemical or process, aerospace etc. which require robust control for higher reliability [27]–[29]. In general, LADRC is used in removing disturbances in single input-single output (SISO) systems. However, the versatility and flexibility of LADRC has led to its utilization for multi-variable decoupling control for non-linear multiple-input multiple-output (MIMO) systems [30]–[32].

A. Fundamentals of LADRC

To explain LADRC, an approximate second order plant is considered in the following form:

$$\ddot{y} = -a_1\dot{y} - a_2 y + w + bu \tag{8}$$

where y is the output, u is the input, and w is the disturbance term which can be a combination of external and internal factors. The second-order plant can be re-written as the following:

$$\begin{aligned}\ddot{y} &= -a_1\dot{y} - a_2 y + w + (b - b_0)u + b_0 u \\ &= f(t, y, \dot{y}, w) + b_0 u\end{aligned} \tag{9}$$

where the lumped term $f(t, y, \dot{y}, w)$ represents the combination of internal dynamics $-a_1\dot{y} - a_2 y + (b - b_0)u$ and the extrenal disturbance w. The term b_0 takes into account the possible disturbances coming from the input signal. It is approximated from nominal values of the energy storage elements in the plant equation.

LADRC principle stipulates that if the lumped disturbances represented by $f(t, y, \dot{y}, w)$ can be estimated (or observed) in real time, they can be actively compensated without the need for a mathematical model. To that end, a linear extended state observer (LESO) is built to observe the states of the system including the disturbance in real time.

1) LESO Observer Design: To observe the second order plant in (9), the following states are defined:

$$x_1 = y, \qquad x_2 = \dot{y}, \qquad x_3 = f(t, y, \dot{y}, w) \tag{10}$$

Additionally, we assume that the dynamics of the disturbance term $h = \dot{f}(t, y, \dot{y}, w)$ is bounded. Therefore, the state space form becomes:

$$\begin{aligned}\dot{x} &= Ax + Bu + Eh \\ y &= Cx\end{aligned} \tag{11}$$

where the state-space matrices are $A = \begin{bmatrix} 0 & 1 & 0 \\ 0 & 0 & 1 \\ 0 & 0 & 0 \end{bmatrix}$, $B = [0 \quad b_0 \quad 0]^{\mathrm{T}}$, $C = [1 \quad 0 \quad 0]$, and $E = [0 \quad 0 \quad 1]^{\mathrm{T}}$. A standard linear Luenberger observer can be designed based on this system:

$$\begin{aligned}\dot{z} &= Az + Bu + L(y - \hat{y}) \\ \hat{y} &= Cz\end{aligned} \tag{12}$$

where L = $[\beta_1 \quad \beta_2 \quad \beta_3]^{\mathrm{T}}$ is the observer gain and z is the observer estimate for the system states x. Using bandwidth parameterization [23], the gains of the observer can be chosen as:

$$\beta_1 = 3\omega_{\mathrm{o}} \quad \beta_2 = 3\omega_{\mathrm{o}}^2 \quad \beta_3 = \omega_{\mathrm{o}}^3 \tag{13}$$

where ω_{o} is the bandwidth of the observer. Higher the ω_{o}, faster the observer. However, in practical implementation, the observer bandwidth is limited by hardware constraints like sensor noises and sampling rates. Since the lumped disturbance is defined as a state, this is also known as extended state observer (ESO).

2) Control law: Once the observer is well tuned, the outputs can track the y, $\dot{y}$ and the lumped disturbance term $\dot{f}(t, y, \dot{y}, w)$ via the terms z_1, z_2, and z_3 respectively. Hence, LADRC actively compensates the influence of the disturbance term by cancelling the z_3 term of the ESO. The control law can be formulated as the following:

$$u = \frac{u_0 - z_3}{b_0} \tag{14}$$

which effectively reduces the second order plant as described in (9) into:

$$\ddot{y} = u_0 \tag{15}$$

which is a straightforward control problem to solve since the steady state error is zero. A simple PD controller of the following form is sufficient:

$$u_0 = k_{\mathrm{p}}(r - z_1) - k_{\mathrm{d}} z_2 \tag{16}$$

The LADRC controller schematic for a second-order plant is shown in Figure 3. However, this approach is not exclusive to second order systems. With few modifications it can be applied to first-order systems as well. In case of first-order plants, the derivative term $\dot{y}$ is absent in the lumped disturbance term $f(t, y, \dot{y}, w)$. Thus, the LESO observes only the state y and the disturbance term. Hence, a proportional controller is sufficient in LADRC control design of first-order plants.

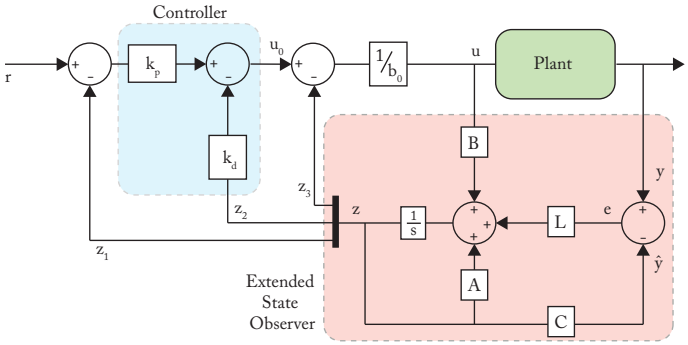

Figure 3: LADRC controller schematic of a second-order plant.

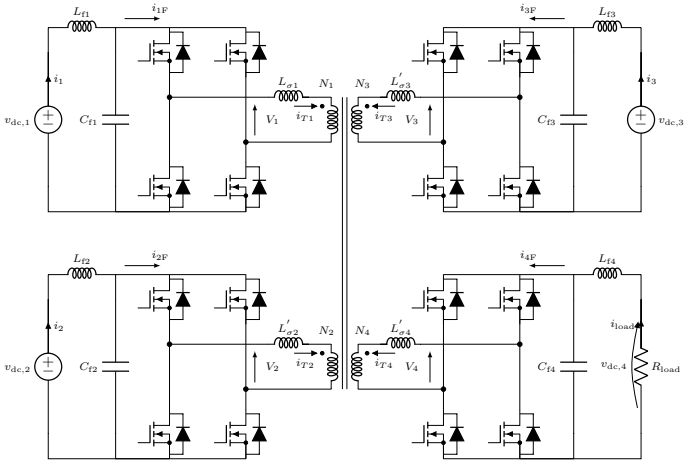

Figure 4: QAB converter schematic for simulation. Port #1, port #2 and port #3 are connected with a voltage source and port #4 is connected with an RC load.

Table I: LADRC formulation of QAB converter ports

System Order	Schematic	Governing equations	LADRC Formulation $\ddot{y}$	f	b_0
1	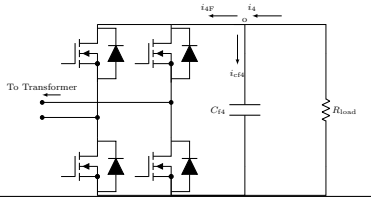	$C_{f4}\dot{v}_{cf,4} = i_4 - i_{4F}$ $i_{4F} = G_{42}\phi_2 + G_{43}\phi_3 + G_{44}\phi_4$	$\dot{V}_{cf4}$	$f_4 = \frac{v_{dc,4}}{C_{f4}R_{load}} - \frac{(G_{42}\phi_2+G_{43}\phi_3)}{C_{f4}} - ...$ $...(\frac{G_{44}}{C_{f4}} - \frac{G_{44,0}}{C_{f4,0}})\phi_4$	$\frac{G_{44,0}}{C_{f4,0}}$
2	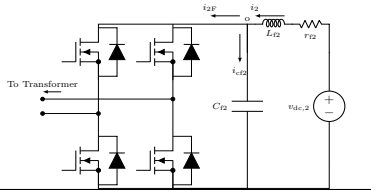	$L_{f2}\dot{i}_2 = v_{dc,2} - v_{cf,2} - r_{f2}i_2$ $C_{f2}\dot{v}_{cf,2} = i_2 - i_{2F}$ $i_{2F} = G_{22}\phi_2 + G_{23}\phi_3 + G_{24}\phi_4$	$\ddot{i}_2$	$f_2 = -\frac{i_2}{L_{f2}C_{f2}} - \frac{r_{f2}}{L_{f2}}\dot{i}_2 + ...$ $...\frac{(G_{23}\phi_3+G_{24}\phi_4)}{L_{f2}C_{f2}} + ...$ $...(\frac{G_{22}}{L_{f2}C_{f2}} - \frac{G_{22,0}}{L_{f2,0}C_{f2,0}})\phi_2$	$\frac{G_{22,0}}{L_{f2,0}C_{f2,0}}$

B. LADRC formulation of QAB converter

Conventional control methods to decouple MIMO interactions like traditional feed-forward compensator [12] require detailed understanding of the term $f(t, y, \dot{y}, w)$ before the control design can be carried out. Classic LADRC approach observes the lumped disturbance to a system and actively compensates for it in real-time. Therefore, LADRC can be used as decoupling control of a MIMO system like multi-active bridge (MAB) converter by modeling the inherent coupling as an observable disturbance. A SISO ADRC controller is then designed for each port of the converter. A four-port MAB converter or a quad-active bridge converter (QAB) is shown in Figure 4. The QAB converter comprises of four ports: three bi-directional voltage sourced ports, and a load port consisting of a resistor in parallel with a capacitor. In the control system, there are three control loops: two current loops for the bi-directional voltage sources in port #2 and port #3; and a voltage control loop for the resistive load in port #4 with R_{load}. This particular combination is selected as it includes the two typical operation modes. Therefore, it is representative and generic. Designing SISO LADRC controllers for each port requires information about the order of that port. The order of a port is decided by the order of the dc side filter. Thus, current controlled ports (#2 and #3) with LC filter are second order plants and the RC load port is a first order plant. The LADRC formulation described in Section III is applied to the individual port control loops of the QAB converter. Table I summarizes the governing equations and the equivalent expressions of the LADRC parameters (f, b_0) of the QAB converter ports. The mathematical equations describing the LADRC formulation of the individual QAB ports are presented in the Appendix.

C. Controller design and observer parameterization

Well-tuned observers can track the coupling disturbance terms ($f_{2,3,4}$) in the system dynamics of the QAB converter ports. Thus, the control inputs of $\phi_2 = \dfrac{u_{i2} - f_2}{b_{2,0}}$, $\phi_3 = \dfrac{u_{i3} - f_3}{b_{3,0}}$, and $\phi_4 = \dfrac{u_{v4} + f_4}{b_{4,0}}$, reduces the the individual port dynamics to:

$$\ddot{i}_2 = u_{i2}, \quad \ddot{i}_3 = u_{i3}, \quad \dot{v}_{dc,4} = u_{v4} \tag{17}$$

All the above systems have no steady state error and therefore can be easily controlled by a P controller or a PD controller depending on the system order. Hence, the control laws for the current loops and the voltage loop can be written as:

$$u_i = k_{pc}(r_c - z_{c1}) - k_{dc}z_{c2} \tag{18}$$

$$u_v = k_{pv}(r_v - z_{v1}) \tag{19}$$

where k_p, k_d are the proportional and the derivative gains of the controllers.

The open loop transfer functions of the individual systems along with the controllers can be expressed as:

$$G_{OL,i} = \frac{k_{pc} + sk_{dc}}{s^2}e^{-s\tau} \tag{20}$$

$$G_{OL,v} = \frac{k_{pv}}{s}e^{-s\tau} \tag{21}$$

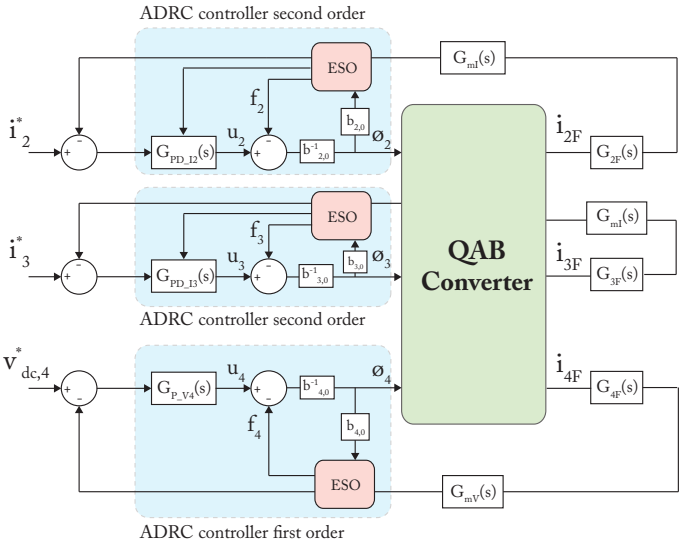

Figure 5: Linear active disturbance rejection decoupling control (LADRC) schematic of QAB converter.

where $e^{-s\tau}$ is the inherent delay associated with practical implementation of the system. For digital controllers, the time delay τ can be represented as $\tau = 1.5T_s$, where T_s is the sampling period of the controller. Neglecting the delay term in the open-loop transfer functions, it is evident that the systems are inherently stable since the phase is not crossing -180^o. Further, considering the delay, the gains (k_p,k_d) can easily be tuned to make sure the gain of the transfer function is below 0 dB when the phase is crossing -180^o. Therefore, using LADRC controllers, system stability is relatively easy to ensure. However, it must be noted that the choice of the control gains is limited by the observer bandwidth due to hardware constraints like sampling frequency and sensor noise. Finally, based on the formulation presented the LADRC decoupling control schematic of the QAB converter is shown in Figure 5.

IV. Simulation Results

Dynamic simulations are performed to validate the the effectiveness of the proposed ADRC control in terms of decoupling the power flows. The selected simulation package is MATLAB/Simulink augmented with the PLECS blockset.

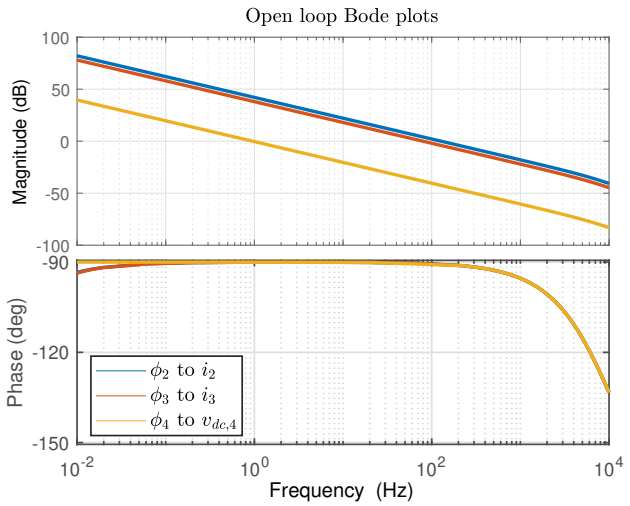

Figure 6: Open loop Bode plots of the QAB control loops.

The QAB converter schematic used for the simulation study is presented in Figure 4. Table II presents the electrical and control specifications of the QAB converter. Further, the performance of ADRC decoupling control is compared with the matrix based conventional decoupling control (CDC). Finally, simulations are also carried out on the QAB converter without any decoupling control, i.e, with only decentralized PI controllers for individual ports. The PI controller for the voltage loop is designed to be slower than the current loops to investigate the interactions between the individual loops. It must be noted that the PI controller gains highlighted in the specifications are applicable to simulations with CDC control and with only PI control. Similarly, in case of LADRC controllers, the voltage loop is designed to be slower. Figure 6 shows the open-loop Bode plots of the individual QAB port control loop gains. The plot is obtained based on (20) and (21) while assuming a delay of 10 µs due to the digital controller. It is evident from the Bode plot that all the sub-systems are inherently stable as the phases are not crossing -180^o.

Dynamic simulations are carried out at the following operating point: P_2 = 800 W; P_3 = -400 W, and $P_{load,4}$ = -740 W. The current set-point of the port #2 is changed from 4A to 2A and the behavior of the current of port #3 and voltage of port #4 are observed to evaluate the performance of the decoupling control strategies.

Figure 7 shows the dynamic waveforms of the relevant QAB port currents and voltages using different control strategies. Figure 7a and 7b show the terminal voltage and current of port #4 while Figure 7c shows the current of port #3. The cross-coupling of the QAB converter control loops is evident from the disturbance caused in the port voltages and currents when no decoupling controller is used. Thus, the dynamic behavior is highly coupled and might lead to stability issues.

The decoupling performance of LADRC controller is evident from the dynamic behavior of the port currents and voltage. The deviations in the transient response of i_3, i_4 and $v_{dc,4}$ are less than 1% compared to 10% in the simulation study without decoupling control. Additionally, the ADRC performance is comparable to the CDC decoupling control, thus validating its performance.

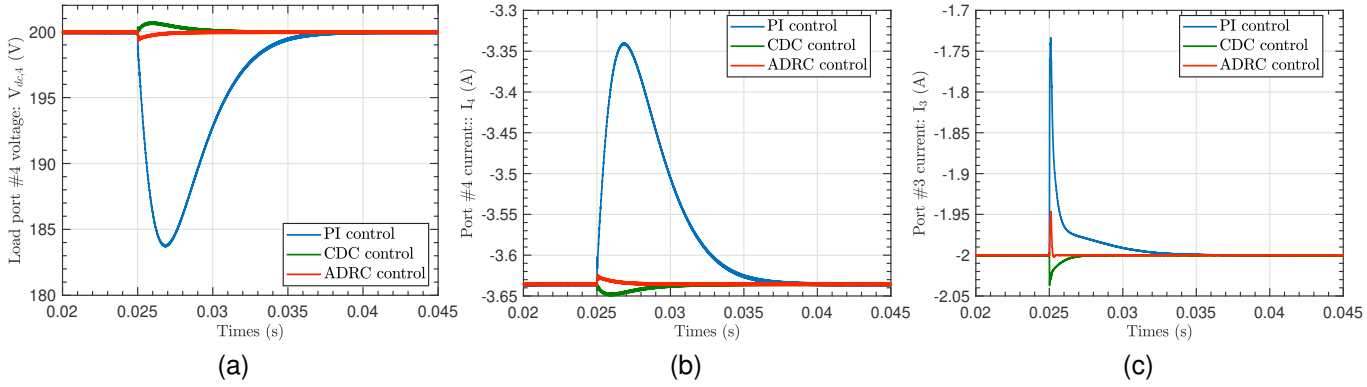

Figure 7: Comparison of decoupling performance of different control strategies; without decoupling control (only PI controllers), conventional decoupling control, and linear active disturbance rejection control during a step-change in set-point of port #2 current i_2 from 4A to 2A. Disturbance in different QAB converter ports: (a) $v_{dc,4}$: voltage of load port #4, (b) i_4: current of load port #4, and (c) i_3: current of port #3.

Table II: Specifications of QAB converter and controllers

Type	Description	Symbol	Unit	Port 1	Port 2	Port 3	Port 4
Electrical parameters	Voltage rating	V_{rated}	V	200	200	200	200
	Current rating	I_{rated}	A	10	10	10	10
	Leakage inductance	L_σ	µH	25	25	25	25
	LC filter inductance	L_{f}	µH	5	5	5	-
	LC filter capacitance	C_{f}	µF	500	500	500	200
	Switching frequency	f_{sw}	kHz	100	100	100	100
	Phase-shift range	ϕ	rad	0	$-\frac{\pi}{2}$ to $\frac{\pi}{2}$	$-\frac{\pi}{2}$ to $\frac{\pi}{2}$	0 to $\frac{\pi}{2}$
ADRC control & observer gains	Observer bandwidth	ω_{o}	rad/s	-	50,000	50,000	50,000
	Proportional	k_{p}	-	-	3	2	0.06
	Differential	k_{d}	-	-	800	500	-
CDC controller PI gains	Proportional	k_{P}	-	-	2.5	1.8	0.06
	Integral	k_{I}	-	-	5000	3000	10

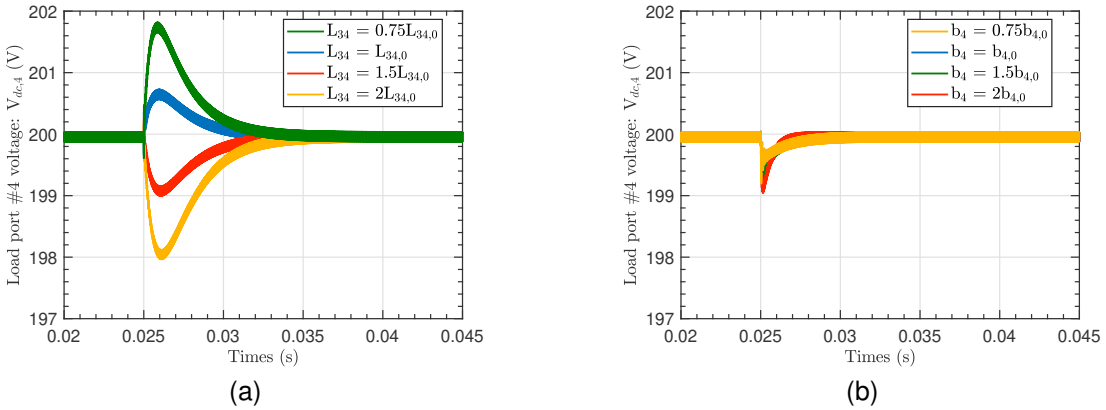

Figure 8: Dynamic behavior of port #4 voltage $v_{\text{dc,4}}$ to investigate sensitivity of decoupling performance to deviation in model parameters: (a) CDC decoupling performance when the value of the link inductance L_{34} is changed in the plant model from it's nominal value $L_{34,0}$, and (b) LADRC decoupling performance when the value of the input gain b_4 is changed from it's nominal value $b_{4,0}$.

Compared to CDC control, LADRC needs less information regarding the plant. The individual port LADRC controllers only require the information regarding the order of the port filter. On the other hand, the centralized CDC control needs internal information of the QAB converter model which includes the nominal values of link inductances between the ports (L_{ij}), rated port voltage ($v_{\text{dc,i}}$), phase shifts during an operating point (ϕ_{ij}) and switching freqeuncy (f_{sw}). Therefore, it is necessary to investigate the decoupling performance of the CDC and LADRC controllers when there is a deviation in values extracted from plant models. The above dynamic simulation is repeated for both the control strategies with deviations in relevant model parameter values. Figure 8a shows the dynamic response of the port #4 voltage $v_{\text{dc,4}}$ using CDC control with deviations in the value of the link inductance between port #3 and #4; L_{34} in the plant model. Similarily, figure 8b shows the decoupling of $v_{\text{dc,4}}$ using LADRC control with deviations in the value of the input gain b_4 in the controller model. The CDC decoupling performance is slightly sensitive to under-compensation or over-compensation depending on the deviation in the nominal value of L_{34} in the QAB plant model. However, in the case of LADRC control, the decoupling performance is robust. It can dynamically decouple the port voltage independent of the deviations in the input gain values in the controller. In practical scenarios, the term b_0 is used as an additional tuning parameter besides observer (ω_{o}) and controller gains.

V. Experimental Validation

A. QAB laboratory setup

Experiments are performed on a quad-active bridge (QAB) converter prototype to demonstrate the dynamic decoupling performance of proposed decoupling strategy. Figure 9 presents the QAB prototype. The overall system consists of four full-bridge modules connected via a high-frequency multi-winding transformer with three bi-directional DC power supplies (SM 500 CP-90 Delta Elektronika) and a resistive load of 55 Ω. Si-C MOSFETs (Wolfspeed C3M0065100K) are used for the full-bridge modules. The high-frequency (HF) multi-winding transformer is implemented by using two stacks of E-70/33/32 cores (core material N87) in parallel and interleaved windings. External leakage inductors of value 25 µH are used to mimic the leakage inductance of the ports. Blocking capacitors are connected to each transformer winding to ensure the transformer is not saturated due to DC bias during transient

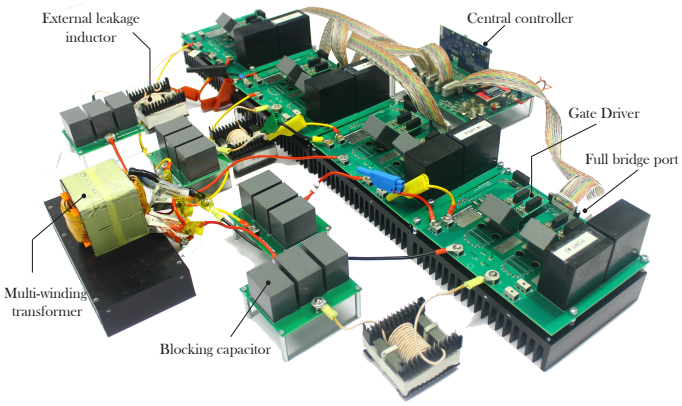

Figure 9: QAB experimental laboratory prototype.

and steady state operating conditions. Finally, the controller is implemented on a Texas Instruments TMS320F28379D DSP.

B. Discrete LADRC implementation and controller tuning

For practical implementation on the microcontroller, a discrete time LADRC formulation is required. The linear extended state observer (LESO) as described in (12) is discretized as the following:

$$\hat{x}(k+1) = \mathbf{A}_\mathrm{d} \cdot \hat{x}(k) + \mathbf{B}_\mathrm{d} u(k) + \mathbf{L} \cdot [y(k) - \mathbf{C}_\mathrm{d} \hat{x}(k)] \quad (22)$$

where $\mathbf{A}_\mathrm{d}$, $\mathbf{B}_\mathrm{d}$ and $\mathbf{C}_\mathrm{d}$ are the discrete-time versions of the state-space model matrices in equation which can be obtained by zero-order-hold (ZOH) discretization [33]:

$$A_\mathrm{d} = I_i + \sum_{i=1}^{\infty} \frac{A^i \cdot T_s^i}{i!}, \quad B_\mathrm{d} = \sum_{i=1}^{\infty} \frac{A^{i-1} \cdot T_s^i}{i!} \cdot B$$
$$C_\mathrm{d} = C, \quad D_\mathrm{d} = D \quad (23)$$

where T_s is the sampling time of the controller, i is the order of the system, and I_i is identity matrix of i-th order. A sampling period of 10 µs is used in the digital controller.

For the first-order plant, the discrete state-space matrcies can be presented as follows:

$$A_\mathrm{d} = \begin{bmatrix} 1 & T_\mathrm{s} \\ 0 & 1 \end{bmatrix}, \quad B_\mathrm{d} = \begin{bmatrix} b_0.T_\mathrm{s} \\ 0 \end{bmatrix}$$
$$C_\mathrm{d} = [1 \quad 0], \quad D_\mathrm{d} = 0 \quad (24)$$

For the second-order plant, the discrete state-space matrcies can be presented as follows:

$$A_\mathrm{d} = \begin{bmatrix} 1 & T_\mathrm{s} & \frac{T_\mathrm{s}^2}{2} \\ 0 & 1 & T_\mathrm{s} \\ 0 & 0 & 1 \end{bmatrix}, \quad B_\mathrm{d} = \begin{bmatrix} b_0.\frac{T_\mathrm{s}^2}{2} \\ b_0.T_\mathrm{s} \\ 0 \end{bmatrix}$$
$$C_\mathrm{d} = [1 \quad 0 \quad 0], \quad D_\mathrm{d} = 0 \quad (25)$$

The individual port controllers are tuned by iteratively increasing the observer bandwidth (ω_o) and the controller gains until either the control signal becomes noisy and leads to oscillations or desired dynamic performance is achieved. After completion of the tuning strategy, an observer bandwidth of 35,000 rad/s is obtained for the second-order LADRC current controllers for ports #2 and #3. For the first order LADRC voltage controller of port #4, an observer bandwidth of 10,000 rad/s is obtained.

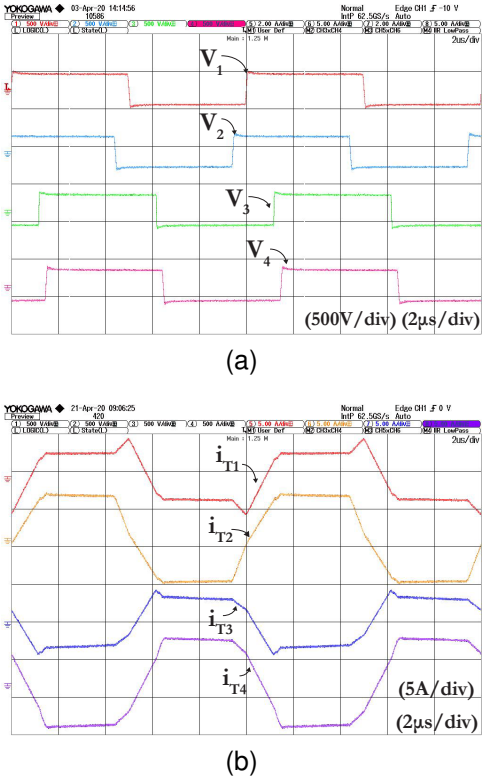

Figure 10: Steady state waveforms of: (a) winding voltages, and (b) winding currents of the QAB converter in 2S-2L mode at operating point: $P_{\mathrm{load},4}$ = -730 W; P_2 = 800 W; P_3 = -400 W.

C. Experimental results

The experimental results consist of the relevant voltage and current waveforms for steady-state and transient operation of the QAB converter using the proposed control strategy.

1) Steady state waveforms: Figure 10 presents the operating steady-state winding current and voltage waveforms of the QAB converter prototype. The operating point is identical to the operating point chosen for the simulation study ($P_{\mathrm{load},4}$ = -730 W; P_2 = 800 W; P_3 = -400 W) where the QAB converter acts in 2 source-2 load (2S-2L) mode.

2) Transient operation waveforms: The dynamic decoupling performance of the proposed control strategy is validated by performing experiments on the prototype at the aforementioned operating point. The port #2 current is changed from 4A to 2A and the behavior of the current of port #3: i_3, and voltage of port #4: $v_{\mathrm{dc},4}$ are observed to evaluate the performance of the decoupling control strategies. Two sets of experiments are conducted: (a) only with PI controllers, and (b) with tuned LADRC decoupling control. Figure 11a shows the transient waveforms of the relevant currents and voltage by only using PI controllers without active disturbance rejection. In this case, the load port voltage ($v_{\mathrm{dc},4}$) is disturbed and drops by 19 V (10% of nominal value) before recovering

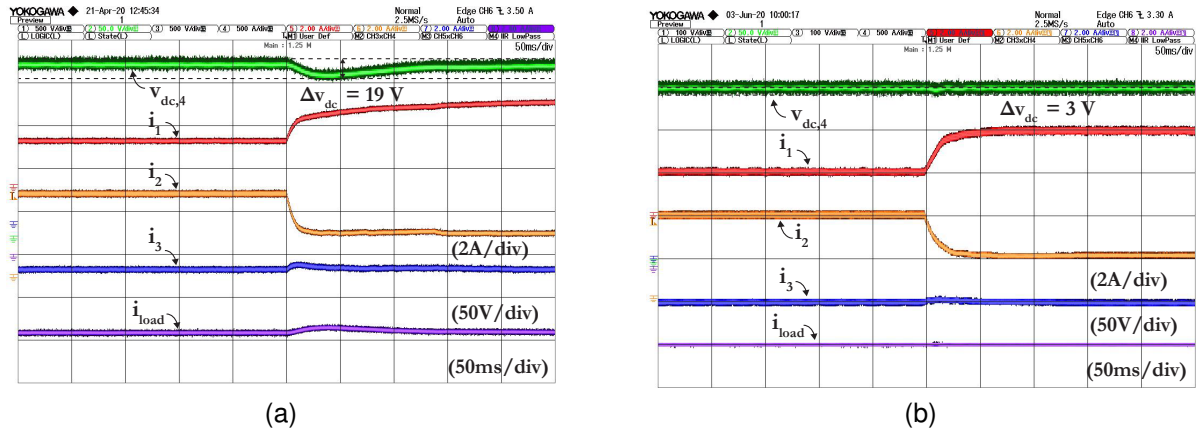

Figure 11: Experimentally obtained dynamic performance of the QAB converter during set-point alteration in port #2: (a) only using PI controllers without ADRC decoupling, and (b) with LADRC decoupling control. LADRC controllers decouple the control loops of $v_{dc,4}$ and i_3 from the coupling disturbance from current loop of i_2. Further, ADRC control achieves zero-steady state error without using integral gain.

to its nominal value. Equivalently, the port #3 current (i_3) is also disturbed due to cross-coupling by 0.4 A (20% of nominal value). Figure 11b shows the transient waveforms of the QAB converter with the proposed LADRC based control. The improvement on the dynamic performance is evident in both the load port voltage $v_{dc,4}$ and port #3 current i_3. The load port current i_{load} is completely decoupled, while the voltage $v_{dc,4}$ only drops by 3 V (1.5% of nominal value). Finally, it must be noted that all the individual LADRC controllers achieve zero-steady state error without using integral gain. In conclusion, the experimental results validate the efficacy of proposed LADRC control for MAB converters in terms of dynamic decoupling performance.

VI. Conclusion

This paper shows that the power flows in a multi-active bridge (MAB) converter can be decoupled in a decentralized manner using minimal system information. Linear active-disturbance rejection control (LADRC) with high bandwidth linear extended state observer (LESO) is used to observe the cross-coupling disturbance, which is then compensated with very short phase delay. This control strategy decomposes the MIMO system into independent single-input single-output (SISO) systems with no mutual interaction allowing power flow control regardless of controller bandwidth. Simulation results show the effectiveness of the proposed control in decoupling the power flows during fast variations. Experiments carried out on a 2 kW 100 kHz four-port MAB converter laboratory prototype validate the control strategy's efficacy. In summary, a well-tuned ADRC controller can dynamically decouple the MAB power flows irrespective of the operating point. Further, system stability is relatively easy to ensure. Compared to the conventional plant matrix-based decoupling control, the proposed control's main advantages are its model-independence and decentralized implementation. Thus, LADRC controlled MAB converters allow scalability without increasing control complexity leading to higher system reliability, flexibility, and robustness.

Appendix

LESO construction for QAB converter

The LADRC formulation of the QAB converter subsystems depend on the order of the system. Port #2 and #3 are the current controlled ports in the QAB converter with LC filter resulting in a second order system. Port #4 is a first order system where the voltage across the capacitor filter is controlled.

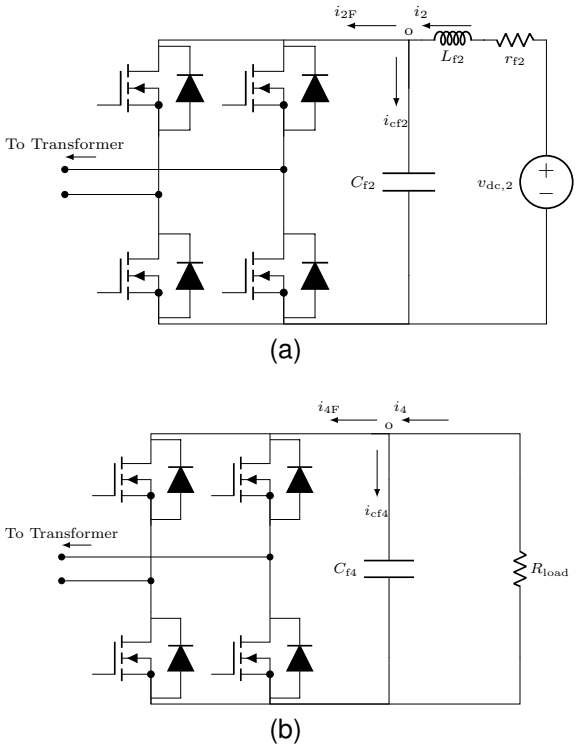

Figure 12: Circuit schematic of QAB converter ports: (a) second order current control port #2 with LC filter, (b) first order voltage control port #4 with only capacitor filter.

Current controlled ports

The LADRC formulation of port #2 is shown here which is also applicable to port #3. Figure 12a shows the circuit schematic of port #2 with the relevant filter current components. The LADRC modelling of a second order plant as shown in section III-A is applied to this port. Applying KVL and KCL at the node O, the following inductor current and capacitor voltage dynamics are obtained:

$$L_{\text{f2}}\frac{\text{d}i_2}{\text{d}t} = V_{\text{dc,2}} - V_{\text{Cf2}} - r_{\text{f2}}i_2 \tag{26}$$

$$\begin{aligned} C_{\text{f2}}\frac{\text{d}V_{\text{Cf2}}}{\text{d}t} &= i_2 - i_{\text{2F}} \\ &= i_2 - (G_{22}\phi_2 + G_{23}\phi_3 + G_{24}\phi_4) \end{aligned} \tag{27}$$

where r_{f2} is the lumped parasitic resistance of the LC filter. Differentiating (26) and combining with (27) the following is obtained:

$$\begin{aligned} \frac{\text{d}^2 i_2}{\text{d}t^2} &= -\frac{1}{L_{\text{f2}}}\frac{\text{d}V_{\text{Cf2}}}{\text{d}t} - \frac{r_{\text{f2}}}{L_{\text{f2}}}\frac{\text{d}i_2}{\text{d}t} \\ &= -\frac{1}{L_{\text{f2}}C_{\text{f2}}}[i_2 - (G_{22}\phi_2 + G_{23}\phi_3 + G_{24}\phi_4)] - \frac{r_{\text{f2}}}{L_{\text{f2}}}\frac{\text{d}i_2}{\text{d}t} \\ &= -\frac{i_2}{L_{\text{f2}}C_{\text{f2}}} - \frac{r_{\text{f2}}}{L_{\text{f2}}}\frac{\text{d}i_2}{\text{d}t} + \frac{G_{23}}{L_{\text{f2}}C_{\text{f2}}}\phi_3 + \frac{G_{24}}{L_{\text{f2}}C_{\text{f2}}}\phi_4 + ... \\ &\quad ...(\frac{G_{22}}{L_{\text{f2}}C_{\text{f2}}} - b_{2,0})\phi_2 + b_{2,0}\phi_2 \\ &= f_2(t, i_2, \dot{i}_2, w_{\text{b}}) + b_{2,0}\phi_2 \end{aligned} \tag{28}$$

where $f_2(t, i_2, \dot{i}_2, w_{\text{b}})$ represents the combined disturbances due to internal dynamics and external disturbances due to the inherent coupling of state i_2 with inputs of other ports ϕ_3 and ϕ_4. The term $b_{2,0}$ can be estimated by the following:

$$b_{2,0} = \frac{G_{22,0}}{L_{\text{f2,0}}C_{\text{f2,0}}} \tag{29}$$

where $G_{22,0}$, $L_{\text{f2,0}}$ and $C_{\text{f2,0}}$ are the nominal values of the parameters G_{22}, L_{f2} and C_{f2}. In theory, LADRC is capable to rejecting uncertainities in estimating $b_{2,0}$.

Based on the methodology introduced in section III-A1, a linear extended-state-observer (LESO) is designed to observe the disturbance $f_2(t, i_2, \dot{i}_2, w_{\text{b}})$:

$$\begin{cases} \dot{z}_{\text{c}} = [A_{\text{c}} - L_{\text{c}}C_{\text{c}}]z_{\text{c}} + [B_{\text{c}} \quad L_{\text{c}}]u_{\text{c}} \\ y_{\text{c}} = z_{\text{c}} \end{cases}$$

where $z_{\text{c}} = [z_{\text{c1}} \quad z_{\text{c2}} \quad z_{\text{c3}}]^{\text{T}}$ is the observer output tracking i_2, $\dot{i}_2$, and $f_2(t, i_2, \dot{i}_2, w_{\text{b}})$ respectively. The state space matrices are $A_{\text{c}} = \begin{bmatrix} 0 & 1 & 0 \\ 0 & 0 & 1 \\ 0 & 0 & 0 \end{bmatrix}$, $B_{\text{c}} = [0 \quad b_{2,0} \quad 0]^{\text{T}}$, $C_{\text{c}} = [1 \quad 0 \quad 0]$. The input vector u_{c} is $[\phi_2 \quad i_2]^{\text{T}}$ and the observer gain vector is L = $[3\omega_{\text{o2}} \; 3\omega_{\text{o2}}^2 \; \omega_{\text{o2}}^3]^{\text{T}}$ where ω_{o2} is the observer bandwidth of port #2.

Voltage controlled ports

The voltage of port #4 is regulated at a nominal value of $V_{\text{dc,load}}$ which is a first order port. The current and the voltage dynamics of the filter as shown in Figure 12b are as follows:

$$\begin{aligned} C_{\text{f4}}\frac{\text{d}V_{\text{cf4}}}{\text{d}t} &= i_4 - i_{\text{4F}} \\ &= \frac{V_{\text{dc,load}}}{R_{\text{load}}} - G_{42}\phi_2 - G_{43}\phi_3 - G_{44}\phi_4 \end{aligned} \tag{30}$$

The goal of the controller is to control the voltage of the house load to a fixed value. It can be acheived by an inner current loop combined with an outer voltage loop. Therefore, the load subsystem can be formulated as an LADRC problem using the same methodology applied in case of the battery subsystem.

The first-order LADRC formulation of the filter dynamics of the load port is as follows:

$$\begin{aligned} \frac{\text{d}V_{\text{dc,4}}}{\text{d}t} &= \frac{V_{\text{dc,4}}}{C_{\text{f4}}R_{\text{load}}} - \frac{1}{C_{\text{f4}}}(G_{42}\phi_2 + G_{43}\phi_3) - \frac{1}{C_{\text{f4}}}G_{44}\phi_4 \\ &= \frac{V_{\text{dc,4}}}{C_{\text{f4}}R_{\text{load}}} - \frac{1}{C_{\text{f4}}}(G_{42}\phi_2 + G_{43}\phi_3) - ... \\ &\quad ...\left(\frac{G_{44}}{C_{\text{f4}}} - b_{4,0}\right)\phi_4 - b_{4,0}\phi_4 \\ &= f_4(t, V_{\text{dc,4}}, w_{\text{b}}) - b_{4,0}\phi_4 \end{aligned} \tag{31}$$

where $f_4(t, V_{\text{dc,4}}, w_{\text{b}})$ represents the combined disturbances due to internal dynamics and external disturbances due to the inherent coupling of state $V_{\text{dc,4}}$ with inputs of other ports ϕ_2 and ϕ_3. Similar to $b_{2,0}$, the input gain term $b_{4,0}$ can be estimated by the following:

$$b_{4,0} = \frac{G_{44,0}}{C_{\text{f4,0}}} \tag{32}$$

Similar to the current controlled ports, a LESO is designed for port #4 to observe $f_4(t, V_{\text{dc,4}}, w_{\text{b}})$:

$$\begin{cases} \dot{z}_{\text{v}} = [A_{\text{v}} - L_{\text{v}}C_{\text{v}}]z_{\text{v}} + [B_{\text{v}} \quad L_{\text{v}}]u_{\text{v}} \\ y_{\text{v}} = z_{\text{v}} \end{cases}$$

where $z_{\text{v}} = [z_{\text{v1}} \quad z_{\text{v2}}]^{\text{T}}$ is the observer output tracking $V_{\text{dc,4}}$, and $f_4(t, V_{\text{dc,4}}, w_{\text{b}})$ respectively. The state space matrices are $A_{\text{v}} = \begin{bmatrix} 0 & 1 \\ 0 & 0 \end{bmatrix}$, $B_{\text{c}} = [b_{4,0} \quad 0]^{\text{T}}$, $C_{\text{c}} = [1 \quad 0]$. The input vector u_{c} is $[\phi_4 \quad V_{\text{dc,4}}]^{\text{T}}$ and the observer gain vector is L = $[2\omega_{\text{o4}} \; \omega_{\text{o4}}^2]^{\text{T}}$ where ω_{o4} is the observer bandwidth of port #4.

ACKNOWLEDGMENT

The authors would like to acknowledge Netherlands Organisation for Scientific Research (NWO) for providing funding for this project.

REFERENCES

[1] A. K. Bhattacharjee, N. Kutkut, and I. Batarseh, "Review of multiport converters for solar and energy storage integration," *IEEE Transactions on Power Electronics*, vol. 34, no. 2, pp. 1431–1445, 2018.

[2] P. Wheeler and S. Bozhko, "The more electric aircraft: Technology and challenges.," *IEEE Electrification Magazine*, vol. 2, pp. 6–12, 2014.

[3] G. Sulligoi, A. Vicenzutti, and R. Menis, "All-electric ship design: From electrical propulsion to integrated electrical and electronic power systems," *IEEE Transactions on Transportation Electrification*, vol. 2, no. 4, pp. 507–521, 2016.

[4] G. Buticchi, L. F. Costa, D. Barater, M. Liserre, and E. D. Amarillo, "A quadruple active bridge converter for the storage integration on the more electric aircraft," *IEEE Transactions on Power Electronics*, vol. 33, no. 9, pp. 8174–8186, 2017.

[5] H. Chen, Z. Hu, H. Luo, J. Qin, R. Rajagopal, and H. Zhang, "Design and planning of a multiple-charger multiple-port charging system for pev charging station," *IEEE Transactions on Smart Grid*, 2017.
[6] M. Vasiladiotis and A. Rufer, "A modular multiport power electronic transformer with integrated split battery energy storage for versatile ultrafast ev charging stations," *IEEE Transactions on Industrial Electronics*, vol. 62, no. 5, pp. 3213–3222, 2014.
[7] J. Schäfer, D. Bortis, and J. W. Kolar, "Multi-port multi-cell dc/dc converter topology for electric vehicle's power distribution networks," in *2017 IEEE 18th Workshop on Control and Modeling for Power Electronics (COMPEL)*, pp. 1–9, IEEE, 2017.
[8] S. Falcones, R. Ayyanar, and X. Mao, "A dc–dc multiport-converter-based solid-state transformer integrating distributed generation and storage," *IEEE Transactions on Power electronics*, vol. 28, no. 5, 2012.
[9] C. Zhao and J. W. Kolar, "A novel three-phase three-port ups employing a single high-frequency isolation transformer," in *Power Electronics Specialists Conference, 2004. PESC 04. 2004 IEEE 35th Annual*, vol. 6, pp. 4135–4141, IEEE, 2004.
[10] Y. Chen, P. Wang, H. Li, and M. Chen, "Power flow control in multi-active-bridge converters: Theories and applications," in *2019 IEEE Applied Power Electronics Conference and Exposition (APEC)*, pp. 1500–1507, IEEE, 2019.
[11] R. W. De Doncker, D. M. Divan, and M. H. Kheraluwala, "A three-phase soft-switched high-power-density dc/dc converter for high-power applications," *IEEE transactions on industry applications*, vol. 27, no. 1, pp. 63–73, 1991.
[12] C. Zhao, S. D. Round, and J. W. Kolar, "An isolated three-port bidirectional dc-dc converter with decoupled power flow management," *IEEE transactions on power electronics*, vol. 23, pp. 2443–2453, 2008.
[13] H. Tao, A. Kotsopoulos, J. Duarte, and M. Hendrix, "A soft-switched three-port bidirectional converter for fuel cell and supercapacitor applications," in *PESC'05. 36th*, pp. 2487–2493, IEEE, 2005.
[14] L. Wang, Z. Wang, and H. Li, "Asymmetrical duty cycle control and decoupled power flow design of a three-port bidirectional dc-dc converter for fuel cell vehicle application," *IEEE Transactions on Power Electronics*, vol. 27, no. 2, pp. 891–904, 2011.
[15] H. Matsuo, W. Lin, F. Kurokawa, T. Shigemizu, and N. Watanabe, "Characteristics of the multiple-input dc-dc converter," *IEEE Transactions on Industrial Electronics*, vol. 51, no. 3, pp. 625–631, 2004.
[16] J. Han, "From pid to active disturbance rejection control," *IEEE transactions on Industrial Electronics*, vol. 56, no. 3, pp. 900–906, 2009.
[17] B. Sun and Z. Gao, "A dsp-based active disturbance rejection control design for a 1-kw h-bridge dc-dc power converter," *IEEE Transactions on Industrial Electronics*, vol. 52, no. 5, pp. 1271–1277, 2005.
[18] J. Wang, S. Li, J. Yang, B. Wu, and Q. Li, "Extended state observer-based sliding mode control for pwm-based dc–dc buck power converter systems with mismatched disturbances," *IET Control Theory & Applications*, vol. 9, no. 4, pp. 579–586, 2015.
[19] J. Yang, H. Cui, S. Li, and A. Zolotas, "Optimized active disturbance rejection control for dc-dc buck converters with uncertainties using a reduced-order gpi observer," *IEEE Transactions on Circuits and Systems I: Regular Papers*, vol. 65, no. 2, pp. 832–841, 2018.
[20] S. Li, J. Yang, W.-H. Chen, and X. Chen, "Generalized extended state observer based control for systems with mismatched uncertainties," *IEEE Transactions on Industrial Electronics*, vol. 59, no. 12, pp. 4792–4802, 2012.
[21] Y. Huang and W. Xue, "Active disturbance rejection control: methodology and theoretical analysis," *ISA transactions*, vol. 53, no. 4, pp. 963–976, 2014.
[22] K. Zhao, J. Zhang, D. Ma, and Y. Xia, "Composite disturbance rejection attitude control for quadrotor with unknown disturbance," *IEEE Transactions on Industrial Electronics*, vol. 67, no. 8, pp. 6894–6903, 2019.
[23] Z. Gao, "Scaling and bandwidth-parameterization based controller tuning," in *Proceedings of the American control conference*, vol. 6, pp. 4989–4996, 2006.
[24] H. Sira-Ramírez, J. Linares-Flores, C. García-Rodríguez, and M. A. Contreras-Ordaz, "On the control of the permanent magnet synchronous motor: an active disturbance rejection control approach," *IEEE Transactions on Control Systems Technology*, vol. 22, no. 5, 2014.
[25] P. Wang, Y. Chen, Y. Elasser, and M. Chen, "Small signal model for very-large-scale multi-active-bridge differential power processing (mab-dpp) architecture," in *Workshop on Control and Modeling for Power Electronics*, IEEE, 2019.
[26] G. Herbst, "Practical active disturbance rejection control: Bumpless transfer, rate limitation, and incremental algorithm," *IEEE Transactions on Industrial Electronics*, vol. 63, no. 3, pp. 1754–1762, 2015.
[27] W.-H. Chen, J. Yang, L. Guo, and S. Li, "Disturbance-observer-based control and related methods—an overview," *IEEE Transactions on Industrial Electronics*, vol. 63, no. 2, pp. 1083–1095, 2015.
[28] W. Xue, W. Bai, S. Yang, K. Song, Y. Huang, and H. Xie, "Adrc with adaptive extended state observer and its application to air–fuel ratio control in gasoline engines," *IEEE Transactions on Industrial Electronics*, vol. 62, no. 9, pp. 5847–5857, 2015.
[29] Y. Zuo, X. Zhu, L. Quan, C. Zhang, Y. Du, and Z. Xiang, "Active disturbance rejection controller for speed control of electrical drives using phase-locking loop observer," *IEEE Transactions on Industrial Electronics*, vol. 66, no. 3, pp. 1748–1759, 2018.
[30] D. Wu and K. Chen, "Design and analysis of precision active disturbance rejection control for noncircular turning process," *IEEE Transactions on Industrial Electronics*, vol. 56, no. 7, pp. 2746–2753, 2009.
[31] J. Su, W. Qiu, H. Ma, and P.-Y. Woo, "Calibration-free robotic eye-hand coordination based on an auto disturbance-rejection controller," *IEEE Transactions on Robotics*, vol. 20, no. 5, pp. 899–907, 2004.
[32] J. Vincent, D. Morris, N. Usher, Z. Gao, S. Zhao, A. Nicoletti, and Q. Zheng, "On active disturbance rejection based control design for superconducting rf cavities," *Nuclear Instruments and Methods in Physics Research Section A: Accelerators, Spectrometers, Detectors and Associated Equipment*, vol. 643, no. 1, pp. 11–16, 2011.
[33] Z. Gajic, *Linear dynamic systems and signals*. Prentice Hall/Pearson Education Upper Saddle River, 2003.

Soumya Bandyopadhyay (S'16) received the B.Tech. degree (First Class Honors) in electrical and electronics engineering from the Jadavpur University, Kolkata, India, in 2011 and the M.Sc. degree in electrical engineering in 2015 from the Delft University of Technology, Delft, The Netherlands. Since 2016, he has been working toward a PhD degree in the field of key power electronics in low voltage dc distribution systems. His research interests include design and control of multi-port dc-dc converter design for renewable sources and storages, smart charging of Electric Vehicles, and multi-objective design optimization of wireless power transfer systems.

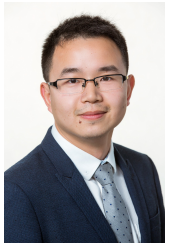

Zian Qin (M'15-SM'19) received the B.Eng. degree in Automation from Beihang University, Beijing, China, in 2009, M.Eng. degree in Control Science and Engineering from Beijing Institute of Technology, Beijing, China, in 2012, and Ph.D. degree from Aalborg University, Aalborg, Denmark, in 2015.

He is currently an Assistant Professor in Delft University of Technology, Delft, Netherlands. In 2014, he was a Visiting Scientist at Aachen University, Aachen, Germany. From 2015 to 2017, he was a Postdoctoral Research Fellow in Aalborg University. His research interests include wide bandgap devices, power electronics based grid and Power2X. He serves as the technical programm chair of IEEE-ISIE 2020, technical program co-chair of IEEE-COMPEL 2020, industrial session co-chair of ECCE-Asia 2020.

Pavol Bauer (SM'07) is currently a full Professor with the Department of Electrical Sustainable Energy of Delft University of Technology and head of DC Systems, Energy Conversion and Storage group. He received Masters in Electrical Engineering at the Technical University of Kosice (a85), Ph.D. from Delft University of Technology (a95) and title prof. from the president of Czech Republic at the Brno University of Technology (2008) and Delft University of Technology (2016). He published over 72 journal and almost 300 conference papers in my field (with H factor Google scholar 43, Web of science 20), he is an author or co-author of 8 books, holds 4 international patents and organized several tutorials at the international conferences. He has worked on many projects for industry concerning wind and wave energy, power electronic applications for power systems such as Smarttrafo; HVDC systems, projects for smart cities such as PV charging of electric vehicles, PV and storage integration, contactless charging; and he participated in several Leonardo da Vinci and H2020 EU projects as project partner (ELINA, INETELE, E-Pragmatic) and coordinator (PEMCWebLab.com-Edipe, SustEner, Eranet DCMICRO).